OPEN

Correspondence and
requests for materials
should be addressed to
N.I.Z. (nzheludev@ntu.
edu.sg)

Planar super-oscillatory lens for sub-diffraction optical needles at violet wavelengths

Guanghui Yuan[1], Edward T. F. Rogers[2,3], Tapashree Roy[2], Giorgio Adamo[1], Zexiang Shen[1] & Nikolay I. Zheludev[1,2]

[1]Centre for Disruptive Photonic Technologies, Nanyang Technological University, Singapore 637371, Singapore, [2]Optoelectronics Research Centre and Centre for Photonic Metamaterials, University of Southampton, Southampton, United Kingdom, [3]Institute for Life Sciences, University of Southampton, Southampton, United Kingdom.

Planar optical lenses are fundamental elements of miniaturized photonic devices. However, conventional planar optical lenses are constrained by the diffraction limit in the optical far-field due to the band-limited wavevectors supported by free-space and loss of high-spatial-frequency evanescent components. As inspired by Einstein's radiation 'needle stick', electromagnetic energy can be delivered into an arbitrarily small solid angle. Such sub-diffraction optical needles have been numerically investigated using diffractive optical elements (DOEs) together with specially polarized optical beams, but experimental demonstration is extremely difficult due to the bulky size of DOEs and the required alignment precision. Planar super-oscillatory lenses (SOLs) were proposed to overcome these constraints and demonstrated that sub-diffraction focal spots can actually be formed without any evanescent waves, making far-field, label-free super-resolution imaging possible. Here we extend the super-oscillation concept into the vectorial-field regime to work with circularly polarized light, and experimentally demonstrate, for the first time, a circularly polarized optical needle with sub-diffraction transverse spot size (0.45λ) and axial long depth of focus (DOF) of 15λ using a planar SOL at a violet wavelength of 405 nm. This sub-diffraction circularly polarized optical needle has potential applications in circular dichroism spectroscopy, super-resolution imaging, high-density optical storage, heat-assisted magnetic recording, nano-manufacturing and nano-metrology.

I t's commonly believed that the smallest achievable focal spot in the optical far-field is constrained by the Abbe diffraction limit. The underlying physical principle for this limit is that the evanescent fields carrying spatial frequencies beyond the highest wavevector in the propagation medium only exist in the near-field region and rapidly decay within a distance of the order of one wavelength. Therefore, in the past decade, much effort has been devoted to achieving super-resolution far-field focusing and imaging by recovery of the non-propagating evanescent fields. This is achieved by specially designed optical devices, such as the negative-index superlens[1], microsphere-based nanolens[2] and hyperlens[3]. However, the super-resolution focal spots obtained using these techniques are formed only in the near proximity of the lens which means that the objects to be imaged should be placed just several tens of nanometres away from the lenses. In fact, far-field optical super-resolution can actually be achieved without making use of the evanescent waves. Indirect ways utilizing nonlinear optical techniques such as two-photon fluorescence microscopy[4] and stimulated emission depletion microscopy[5] have demonstrated the improvement of resolution down to sub-diffraction scale by use of luminescent objects, but they work only for narrow classes of specimens. Straightforward methods by means of "super-oscillation" have been proposed to achieve sub-diffraction spot size and overcome the short-working-distance and fluorescence labeling constraints, and thus research in super-oscillation has seen a revival of interest in the photonic community in recent years[6–9].

The pivotal idea of super-oscillation is that a super-resolved hotspot can be formed beyond the optical near-field by the delicate interference of propagating waves with band-limited wavevectors. Mathematically, this is allowable because a band-limited function is able to oscillate much faster than its highest constituent frequency component[7]. In principle, there is no physical limitation on resolution and only a tradeoff in transfer of intensity to sidebands and reduced energy concentration in the hot-spot. Super-oscillatory hot-spots have been generated through amplitude and phase modulation using spatial light modulators (SLMs)[10,11], optical eigenmodes methods[12,13], pupil filters[14,15], binary masks or by planar metamaterials[16]. Binary amplitude modulation masks stand

out among these for their ease of manufacture using existing nano-fabrication technologies such as focused ion beam (FIB) milling and electron beam lithography (EBL). Experimental observations of super-oscillations based on binary masks have been reported using quasi-crystal nanohole arrays[17,18], quasi-periodic and quasi-random masks[19], and binary ring masks[20–23]. The latter ring masks show much higher throughput efficiency and can be optimized in a controllable manner by an iterative algorithm such as binary particle swarm optimization (BPSO). A scanning imaging system based on such sub-diffraction super-oscillatory lenses (SOLs) has also been demonstrated, and resolution better than $\lambda/6$ has been achieved[21]. The point spread function of such SOLs has been experimentally studied as well, showing that they can be directly used as imaging lenses with sub-diffraction resolution[22].

In previous binary SOL-based super-focusing works, linearly polarized beams were commonly used to illuminate the cylindrically symmetric masks. Scalar field approximation gives sufficient accuracy to calculate the diffraction patterns and very good agreement was found between the experimentally recorded images and simulations[20–23]. In fact, the concept of super-oscillation can work with arbitrary polarization state, for example circularly polarized beams and radially polarized beams. Polarization gives an additional degree of freedom to control the properties of the focal spots. In the vectorial regime, SOLs have been numerically demonstrated to focus radially polarized beams, producing longitudinally polarized hot-spots that beat the diffraction limit in the optical far-field[24,25]. However, circularly polarized beams give many advantages when working with SOLs such as: a) easier alignment due to the uniform intensity profile (compared with the doughnut profile for radial polarization); b) cylindrically symmetric polarization states without any depolarization effects after transmission through the SOLs; c) the predominant transverse electric field components of the generated super-oscillatory focal spots are continuous even after passing through dielectric interfaces which is beneficial for optical data storage and photolithography applications; (d) potential applications in circular dichroism spectroscopy to image the optical chirality of molecules and proteins.

The focusing properties of circularly polarized beams with conventional objective lenses combined with have been studied[26,27], and super-resolved focal spots with long DOE, termed "optical needles" hereafter, have been numerically achieved[28]. In a similar way, longitudinally polarized, transversally polarized and linearly polarized optical needles have been produced by tightly focusing a radially polarized beam, azimuthally polarized beam with additional phase hologram, and linearly polarized beam respectively[29–32]. Focal spots with small transverse dimension and long DOF are desirable for many applications: for example in optical storage and nanolithography, where larger data density and better tolerance on the working distance can be anticipated, and in super-resolution imaging of objects with surface roughness. However, the bulky optical elements make experimental implementation difficult due to aberration and system alignment issues. To overcome these limitations, planar and aberration-free far-field focusing devices in the optical and microwave regimes have been reported using plasmonic metasurfaces[33], plasmonic metalenses[34,35], binary Fresnel zone plates and microaxicons[36,37], holey-metal lenses[38,39], and plasmonic bull-eye structures[40]. To our knowledge, the focal spots generated in all these cases are still diffraction-limited. In this work, we experimentally demonstrate the first circular polarization optical needle generator using planar SOLs working near the short wavelength edge ($\lambda=405$ nm) of the visible spectrum. The transverse components of the focal spot are circularly polarized and proven to be super-oscillatory with feature sizes as small as 185 nm ($\sim 0.45\lambda$) which is beyond the conventional Abbe diffraction limit. The DOF is as long as 10λ and can be increased up to 15λ with an appropriate design. It is noted that linearly polarized super-oscillatory optical needles generated by similar SOLs have been reported, where a wavelength of 640 nm was utilized to achieve

spot size around 269 nm[21]. Here, we seek a smaller spot size and better resolution, controllable focal length and longer DOF by reducing the incoming wavelength and extend this technique into the vectorial field regime.

Results

Super-oscillatory circularly polarized optical needle generation. A scanning electron microscopy (SEM) image of the first SOL under study (Sample 1) is shown in Fig. 1(a), and a zoomed-in view of the dashed box is presented in Fig. 1(b). Detailed design parameters (focal length, transverse spot size and DOF of the two samples (Sample 2 will be discussed later) are presented in Supplementary Table S1). At the short wavelength of 405 nm, higher manufacturing accuracy is essential due to the fact that subwavelength focal spots, in principle, are formed by constructive interference of the fields diffracted from the mask and therefore large fabrication discrepancy may lead to significant deviations of experimental data from the original design. From detailed analysis of the SEM images, the standard deviation of the measured slit width is calculated to be around 8.8 nm (see Supplementary Table S2 for more details).

The experimentally recorded electric field distribution within 20 μm propagation distance after Sample 1 is depicted in Fig. 1(c), while the theoretically predicted result is given in Fig. 1(d) for comparison. Excellent agreement can be seen between them: the focal length (central position of the optical needle) is actually found to be $Z_f = 10$ μm, which is identical to the original design; the generation of optical needles ranging from 8 μm to 12 μm (DOF $\sim$ 10λ); sidebands surrounded the needles and other two foci located at $z=16$ μm and $z=18.2$ μm respectively. This agreement indicates that the limited numerical aperture ($NA=0.95$) of the collection objective doesn't significantly distort the diffraction patterns which is consistent with our previous findings[20,23]. Another aspect that needs to be considered is the contributions from plasmonic effects (the excitation of surface plasmon polaritons) to the far-field signals which in our case can be neglected due to the following reasons: the plasmonic waves will attenuate rapidly and only play a dominant role in the near-field region; the gold film thickness is much smaller than the wavelength while the smallest width is around half-wavelength and thus the cavity resonance is insignificant.

To make a comprehensive investigation of the properties of optical needle, we measure the electric field intensity in the transverse cross-sections using a sCMOS camera. Images at different propagation distances of 9 μm, 10 μm and 11 μm within the non-diffracting region of the optical needle are displayed in Figs. 2(a) – (c) respectively, as examples. All the images show similar intensity profiles and reasonable circular symmetry. The theoretical data calculated by Rayleigh-Sommerfeld diffraction integrals (see Methods) at the same propagation distances of 9 μm, 10 μm and 11 μm are presented in Figs. 2(d) – (f) respectively. It is seen that the experimental data are consistent with the theory in that they show bright central main lobe and several surrounding sidelobes with gradually reducing intensity. The peak electric field intensity in the main lobe is at least 5 times larger than that of the sidebands. Line-scans of the intensity distribution along the horizontal line across the focal spot diameter are shown in Figs. 2(g) – (i). The full-width-at-half-maximum (FWHM) of spot size from experiment(theory) for $z=9$ μm, 10 μm and 11 μm are measured to be 208 nm(196 nm), 177 nm(185 nm) and 193 nm(181 nm) respectively. In contrast, the Abbe diffraction limit given by this SOL under scalar field approximation is $\lambda/(2NA)=226$ nm, where $NA=0.89$ is calculated from $n \ast \sin\theta_{max}$, $n=1$ is the refractive index in air and θ_{max} is the maximal focal angle determined by the mask aperture r_{max} and focal length Z_f through the relation $\tan(\theta_{max})=r_{max}/Z_f$; this proves that our SOL is able to break the conventional diffraction limit. Both the designed and measured spot sizes are only slightly smaller than the diffraction limit because
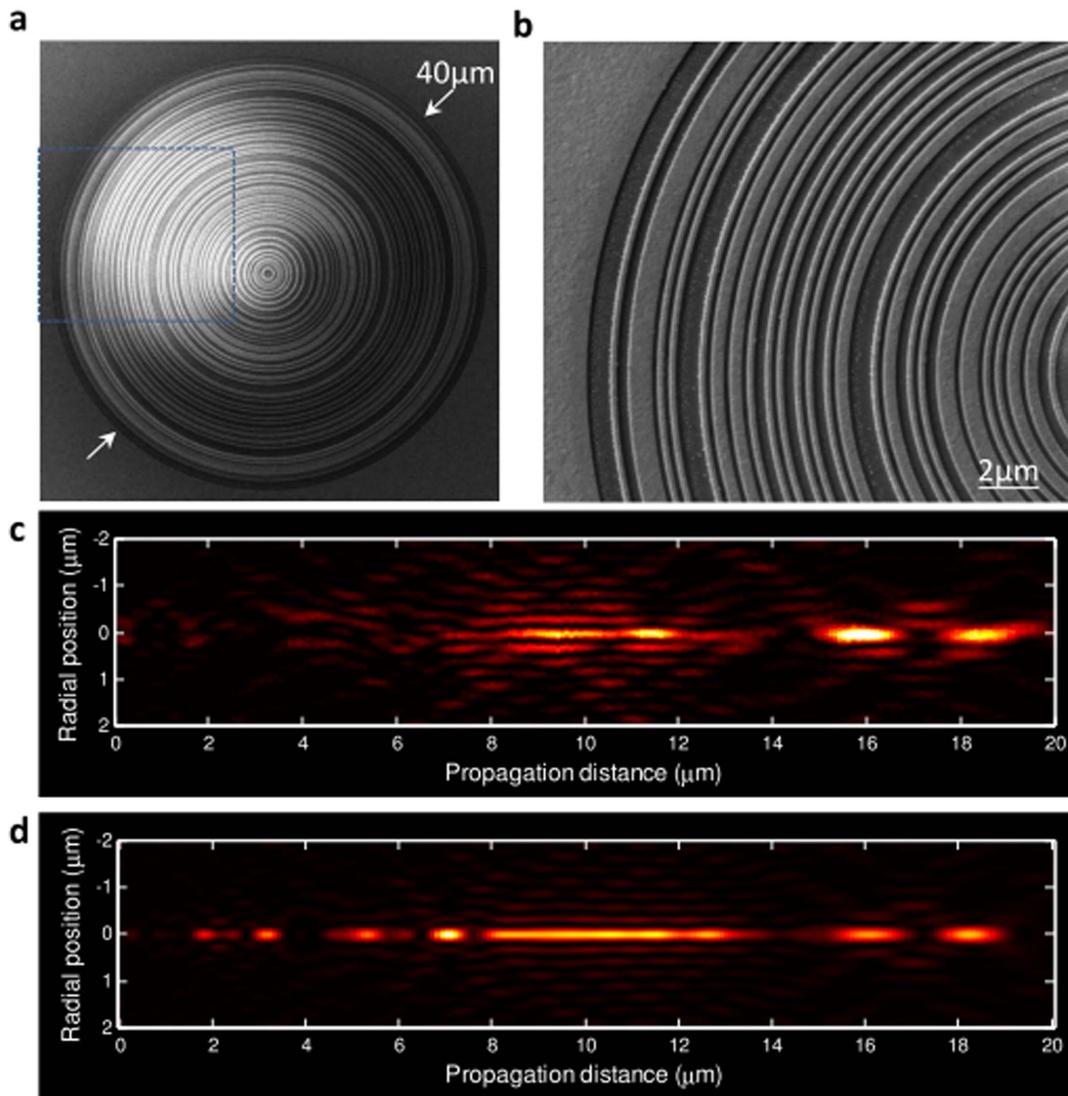
Figure 1 | SOL design and diffraction patterns in longitudinal cross-section. (a), SEM image of the super-oscillatory lens with diameter of 40 μm, which is divided into 100 rings in the radial direction with smallest annulus width of 200 nm. The focal length and DOF are designed to 10 μm and 4 μm respectively. The sample was fabricated by focused ion beam onto a 100 nm-thick gold film deposited on a glass substrate using thermal evaporation; (b), Zoom-in view of the area within the blue dashed box in a, the standard deviation of the measured ring-width is less than 10 nm compared with the design; (c), (d), Experimental and simulated intensity of the diffraction patterns within propagation distance of 20 μm respectively.

the parameters of the SOL are chosen to guarantee a good energy concentration in the mainlobe with a sub-diffraction-limited spot size. It is known that a reduction of the main lobe spot size is always accompanied by an increasing in sideband intensity, which is intrinsic to super-oscillation.
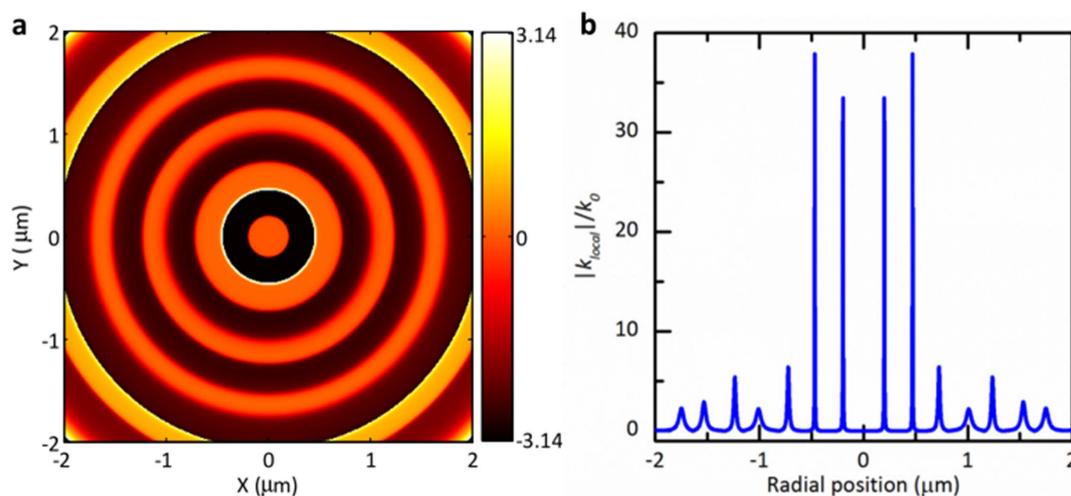
Phase and local wavevector profiles. We also verify here that the generated focal spots are indeed super-oscillatory. According to the definition of super-oscillation[7], the local wavevector ($k_{local} = \nabla\Psi$, phase gradient) in the super-oscillatory region should be larger than the highest wavevector component in the optical fields ($k_0 = 2\pi/\lambda$ in free space). For vectorial fields with complex polarization states, the phase distributions can be simulated from the formula $\Psi = \arg\left(\left\langle \vec{E}\left(\vec{r}_1\right) \middle| \vec{E}\left(\vec{r}_2\right) \right\rangle\right)$, where $\arg(x)$ gives the argument of the complex number x, and $\left\langle \vec{E}\left(\vec{r}_1\right) \middle| \vec{E}\left(\vec{r}_2\right) \right\rangle$ denotes the inner product of two electric field vectors $\vec{E}\left(\vec{r}_1\right)$ and $\vec{E}\left(\vec{r}_2\right)$ at two observation points $\vec{r}_1$ and $\vec{r}_2$ on the wavefront. Here we use the central position as the reference point. The calculated phase at the

focal plane and line-scan of k_{local} across the diameter are presented in Figs. 3(a) and 3(b) respectively. It is clearly seen that there are several regions where the phase oscillates rapidly and k_{local} is much larger than k_0. These super-oscillatory regions correspond to the intensity minima, which is characteristic of super-oscillation. At the first minimum adjacent to the mainlobe, k_{local} can be larger than $30k_0$ and therefore, the hot-spot is being squeezed by the super-oscillatory region into a spot smaller than the conventional diffraction limit.
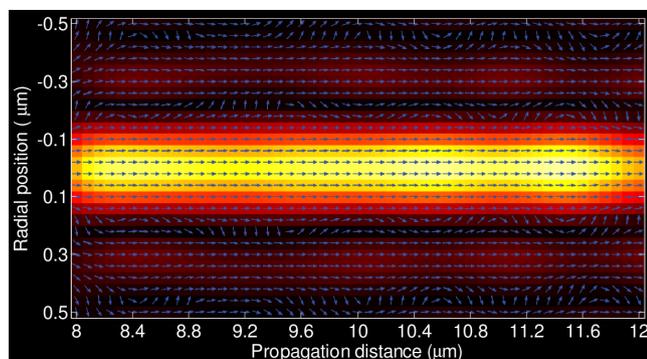
Poynting vector distributions. In order to better understand the mechanism forming the circular polarization optical needle, we plotted the Poynting vectors near the DOF range (from 8 μm to 12 μm), as shown in Fig. 4. The time-averaged Poynting vector is calculated by $\left\langle \vec{s} \right\rangle = \frac{1}{2}\operatorname{Re}\left(\vec{E} \times \vec{H}*\right)$, where the asterisk denotes the complex conjugation. It is seen that within the main lobe, the Poynting vector is almost homogeneous and the axial component of $\left\langle \vec{s} \right\rangle$ plays a dominant role in shaping the overall profile. This indicates that the optical energy confined in the central focal spot will be transported efficiently along the propagation direction, which is
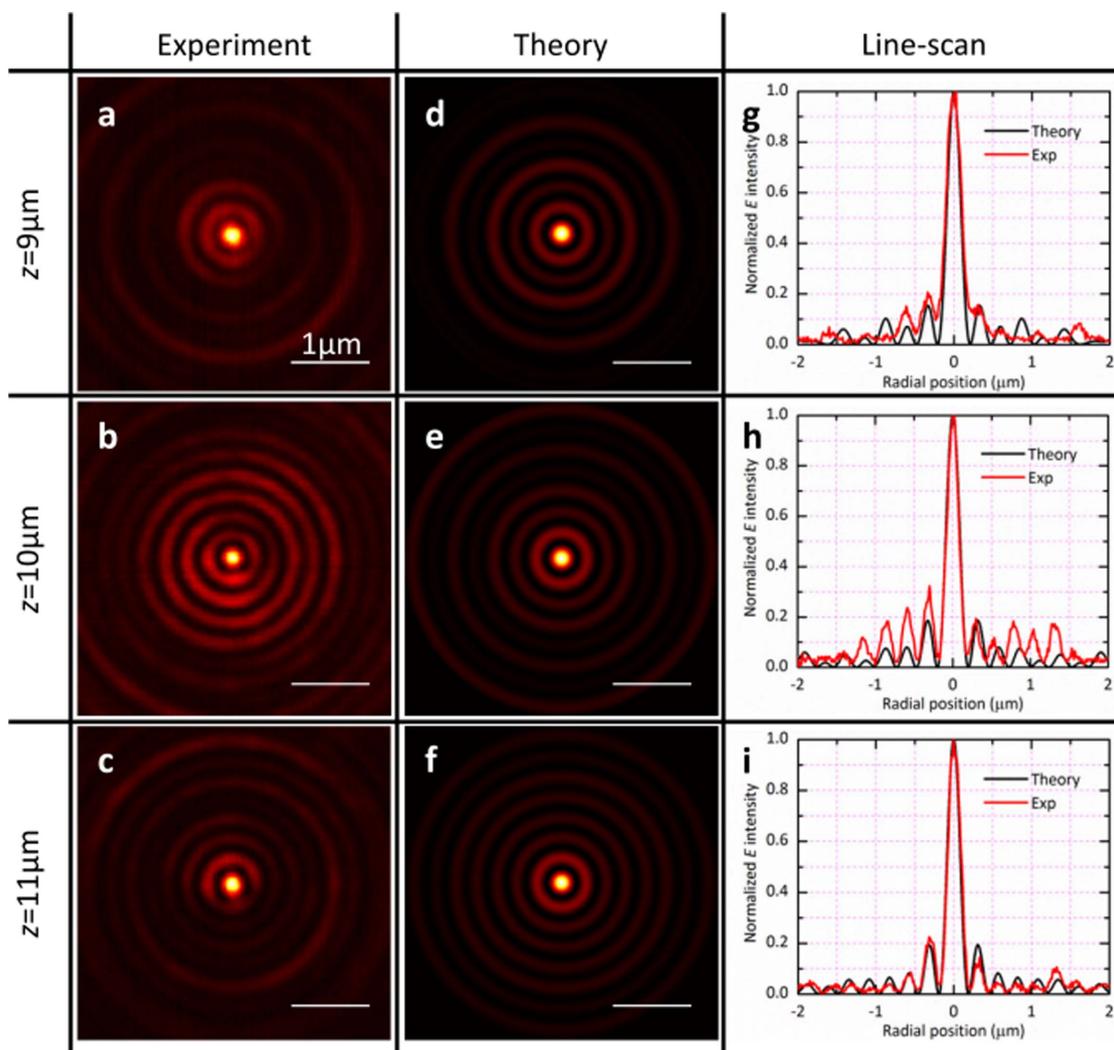
Figure 2 | Transverse electric field intensity profiles. (a–c), Experimentally recorded and (d-f) theoretically calculated diffraction patterns at the propagation distances of $z=9$ μm (top row), 10 μm (middle row) and 11 μm (bottom row) within the generated optical needle. The contrastive line-scan distributions along the horizontal line across the focal spot center are shown in (g) to (i) respectively.

Figure 3 | Phase and local wavevector profiles in focal plane. (a), Phase distributions at $z=10$ μm, where the central point is used as reference; (b), Local wave-vector distributions along radial direction. The peaks indicate the super-oscillatory regions where k_{local} is larger than k_0 and the phase oscillates very rapidly.

Figure 4 | Normalized Poynting vector distributions in the longitudinal cross-section. In the optical needle region, the Poynting vectors within the mainlobe almost point to the axial direction, indicating the energy flow along propagation. At the super-oscillation regions, the Poynting vectors change their directions rapidly, corresponding to a small amount of energy exchange between the optical needle and the first sidelobes.

very different from the case of longitudinally polarized optical needle generated by a highly focused radially polarized beam, where the predominant longitudinally polarized electric field produces non-propagating energy flow in the transverse plane[29]. Another phenomenon to be observed is that the energy flows in the super-oscillatory regions change their directions rapidly although the electric field intensities in the super-oscillatory regions are weak and the magnitude of the Poynting vectors is small, which indicates a small exchange of electromagnetic energy between the

optical needle and the first sidelobes during propagation. This can be intuitively understood by considering that, while the energy content of the needle does not change significantly over the depth of focus, some small exchange is probable due to the complex interference needed to create the super-oscillatory needle.

Generating an optical needle with longer DOF. The properties of the circularly polarized optical needle can be flexibly tuned using the BPSO algorithm to achieve, for example, longer DOF. To this regard, we designed and measured a second sample (Sample 2) which has a central block diameter of 12 μm and aims at a DOF of 6 μm (~15λ) at the same focal length as Sample 1 (10 μm). The design with a central-block is helpful to increase the super-oscillation region and make it attractive for large-area super-resolution imaging with suppressed background noise. In this case, objects with sub-diffraction spacing located within the super-oscillatory region can be resolved[11,21,22]. An SEM micrograph of Sample 2 is shown in Fig. 5(a). The experimental and theoretical data are given in Figs. 5(b) and 5(c) respectively. Bright focal spots are formed ranging from $z=7$ μm to 13 μm which agree with the original design very well. This can be seen more clearly from the axial intensity distributions plotted in Fig. 5(d). Although there are some intensity fluctuations within the optical needle, the optical energy is highly confined in these regions. The spot sizes are investigated as well and found to range from 0.41λ to 0.49λ within the optical needle. For example, at discrete propagation distances for $z=8$ μm to 12 μm in step of 1 μm, the FWHMs obtained from experiment(theory) are evaluated to be 0.44 ± 0.021λ(0.45λ), 0.43 ± 0.042λ(0.44λ), 0.44 ± 0.035λ(0.43λ), 0.45 ± 0.042λ(0.43λ) and 0.45 ± 0.042λ(0.43λ) respectively, showing the super-resolution
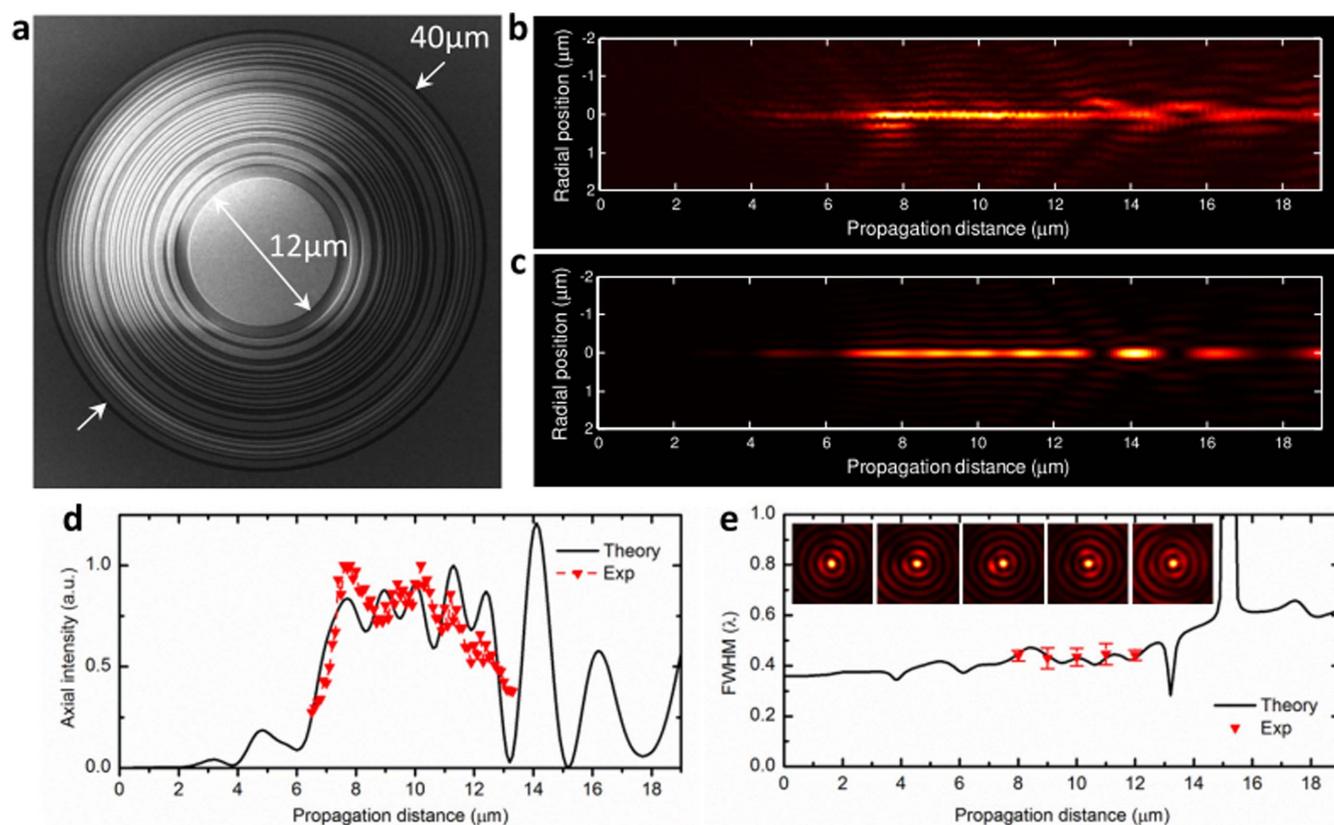
Figure 5 | Central block SOL design for longer DOF. (a), SEM image of Sample 2 which has a central block diameter of 12 μm and is designed with focal length of 10 μm and DOF of 6 μm; (b), (c), Experimental and simulated intensity of the diffraction patterns within propagation distance of 19 μm respectively; (d), Axial intensity distributions from theory (solid line) and experiment (dashed line with symbol); (e), FWHM of the spot in transverse direction: theory (solid line) and experiment (down triangle). The error bar comes from the spot size averaging along x and y directions. Insets show the transverse intensity distributions within area of 2 μm*2 μm at $z=8$ μm to 12 μm in step of 1 μm.

capabilities. We average the spot size along two orthogonal directions to reduce the errors induced by possible polarization impurity of the incoming laser and fabrication imperfections. Insets show the original images captured by the CCD camera within an area of interest of 2 μm*2 μm, where the experimental data were taken.

Discussion

It is important to note that the spot size can be further reduced in combination with higher-refractive-index materials. For example, in oil immersion (refractive index ~1.51), the spot size can be less than 135 nm without apparent distortion of longitudinal needle features (see Supplementary Information for details). Sub-50 nm hot-spots are possible by use of solid-immersion techniques and have been numerically demonstrated for heat-assisted magnetic recording applications[41]. Here, refractive index materials help to reduce the effective wavelength and super-oscillation further squeezes the spot-size down to sub-diffraction level.

Using super-oscillation, longitudinally polarized super-oscillatory optical needles can be generated using radially polarized light, but direct detection is more difficult through far-field measurements (as used here) because the longitudinal component is non-propagating and is related to energy flow in the transverse plane. Other techniques, for example exposure of photoresist or fluorescence with proper orientation may be used, but are outside the scope of this work.

To sum up, we show the first experimental demonstration of a circularly polarized optical needle using a planar super-oscillatory binary mask and violet-wavelength circularly polarized excitation beam. The transverse spot size is reduced to a sub-diffraction scale (0.45λ) while the axial DOF is as long as 15λ. The typical focal length can be up to 10 μm and allows a larger working distance. The Poynting vectors near the optical needle regions are calculated, where the axial energy flows in the hot-spots are confirmed and shown to be uniform. Planar and thin SOLs are desirable for fabrication ease as well as for integration simplicity. This circularly polarized super-oscillatory optical needle promises broad and practical applications in heat-assisted magnetic recording, high-density optical data storage, photolithography, super-resolution imaging of objects with surface roughness or optical chirality of molecules by circular dichroism[42], spatially resolved Raman imaging, optical coherence tomography imaging, nano-manufacturing and nano-metrology.

Methods

Sample design and optimization. The design of such mask is based on the powerful binary particle swarm optimization (BPSO) algorithm[43]. The target function is defined as $\exp\left(-\dfrac{r^2}{a^2}\right)\exp\left(-\dfrac{(Z-Z_f)^{10}}{b^{10}}\right)$, where Z_f is the focal length, $a = \dfrac{FWHM}{2\sqrt{\ln 2}}$, $b = \dfrac{DOF}{2\sqrt{\ln 2}}$, $FWHM$ is the full-width half maximum of transverse spot size and DOF is the depth of focus. A super-Gaussian function is used to describe the extended longitudinal profile of optical needle. The optimum mask design has minimal variance between the actual field distribution and the merit function.

Theoretical calculation of diffraction pattern. The electric fields diffracted by a circularly symmetric mask illuminated by a left-handed circularly polarized beam can be derived from the Rayleigh-Sommerfeld integrals[44]:

$$E_x(\rho,\theta,z) = \frac{-1}{2\pi}\iint A(r) \times \frac{\partial}{\partial z}\left[\frac{e^{ikR}}{R}\right]rdrd\varphi \tag{1}$$

$$E_y(\rho,\theta,z) = \frac{-1}{2\pi}\iint A(r) \times \frac{\partial}{\partial z}\left[\frac{e^{ikR}}{R}\right]rdrd\varphi \tag{2}$$

$$E_z(\rho,\theta,z) = \frac{1}{2\pi}\iint A(r)\left[re^{i\varphi} - \rho e^{i\theta}\right] \times \frac{1}{R}\frac{\partial}{\partial R}\left[\frac{e^{ikR}}{R}\right]rdrd\varphi \tag{3}$$

where $A(r)$ is the initial amplitude of incident beam before the mask, $R^2 = z^2 + \rho^2 + r^2 - 2\rho r\cos(\varphi-\theta)$, (ρ,θ,z) and $(r,\varphi,0)$ are the cylindrical coordinates in the observation plane and mask plane respectively. E_y and E_x have identical intensity profile and a

phase difference of π/2, indicating that the electric field in the transverse (xy) plane after diffraction is still circularly polarized. In order to make quantitative comparisons between the experimental data and theoretical prediction, we do not consider the longitudinal component E_z in the main text because far-field measurements (like the images taken by sCMOS camera) are limited to the transverse components of the electric fields and E_z is always strongly suppressed in the image plane due to polarization filtering[45]. The magnetic fields can be rigorously calculated from Maxwell's equation as

$$\vec{H} = \frac{i}{\omega\mu_0}\nabla\times\vec{E} = \frac{i}{\omega\mu_0}\left[\left(\frac{\partial E_z}{\partial y} - \frac{\partial E_y}{\partial z}\right)\vec{e}_x + \left(\frac{\partial E_x}{\partial z} - \frac{\partial E_z}{\partial x}\right)\vec{e}_y + \left(\frac{\partial E_y}{\partial x} - \frac{\partial E_x}{\partial y}\right)\vec{e}_z\right] \tag{4}$$

Sample preparation. The SOL is fabricated by focused ion beam (Helios 650, 30 kV, 24pA) milling through a 100nm-thick gold film deposited on a glass substrate using thermal evaporator (Oerlikon Univex 250). The mask (diameter 40 μm) is divided into 100 concentric annuli each with either unit or zero transmittance and the smallest annulus width is 200 nm.

Experimental apparatus. The experimental setup is based on a customized Nikon dual-mode microscope, where a high magnification and high-NA objective (Nikon CFI LU Plan APO EPI 150X, NA=0.95) together with a 4X magnification changer collect the diffraction pattern and then project it onto a high-resolution sCMOS camera (Andor Neo, 2560*2160, pixel size 6.5 μm). A linearly polarized incident beam (Toptica Photonics AG, IBEAM-Smart-405-S) was first converted to circular polarization using a quarter-waveplate, then expanded by 5 times using a telescope system (combination of two confocal convex lenses with focal lengths of 15 mm and 75 mm), and finally illuminated the SOL from the substrate side.

Optical far-field characterization. Since the subwavelength focal spots are formed by interference of propagating waves, they can be directly imaged by a conventional optical microscope and mapped into the far-field. (See the Supplementary Figure S2 for detailed optical configuration.) Under 600X magnification, the effective pixel size of the sCMOS camera is around 13 nm, which is inferred from the microscope images of the SOL sample under white light illumination and is fine enough to reconstruct the subwavelength focal spots. The longitudinal cross-section distributions were captured by scanning the SOL in the z direction on a Labview controlled piezo nanopositioning stage (PI E517) with step size of 100 nm. The transverse cross-section distributions at specific propagation distances were captured directly by the sCMOS camera after obtaining the longitudinal cross-section distributions. Due to the mechanical drift of the imaging system which becomes prominent at high magnification, there is slight movement of the focal spots in the transverse direction when mapping the electric field in the longitudinal plane. We reduce this issue by re-centering of focal spots during post-processing.

1. Zhang, X. & Liu, Z. W. Superlenses to overcome the diffraction limit. *Nat. Mater.* **7**, 435–441 (2008).

2. Wang, Z. B., Guo, W., Li, L., Luk'yanchuk, B., Khan, A., Liu, Z., Chen, Z. C. & Hong, M. H. Optical virtual imaging at 50 nm lateral resolution with a white-light nanoscope. *Nat. Commun.* **2**, 218 (2011).

3. Rho, J., Ye, Z. L., Xiong, Y., Yin, X. B., Liu, Z. W., Choi, H., Bartal, G. & Zhang, X. Spherical hyperlens for two-dimensional sub-diffractional imaging at visible frequencies. *Nat. Commun.* **1**, 143 (2010).

4. Denk, W., Strickler, J. & Webb, W. Two-photon laser scanning fluorescence microscopy. *Science* **248**, 73–76 (1990).

5. Hell, S. W. & Wichmann, J. Breaking the diffraction resolution limit by stimulated emission: stimulated-emission-depletion fluorescence microscopy. *Opt. Lett.* **19**, 780–782 (1994).

6. Zheludev, N. I. What diffraction limit?". *Nat. Mater.* **7**, 420–422 (2008).

7. Berry, M. V. & Popescu, S. Evolution of quantum superoscillations and optical superresolution without evanescent waves. *J. Phys. A: Math. Gen.* **39**, 6965–6977 (2006).

8. Greenfield, E., Schley, R., Hurwitz, I., Nemirovsky, J., Markris, K. G. & Segev, M. Experimental generation of arbitrarily shaped diffractionless superoscillatory optical beams. *Opt. Express* **21**, 13425–13435 (2013).

9. Markris, K. G. & Psaltis, D. Superoscillatory diffraction-free beams. *Opt. Lett.* **36**, 4335–4337 (2011).

10. Huang, F. M. & Zheludev, N. I. Super-resolution without evanescent waves. *Nano Lett.* **9**, 1249–1254 (2009).

11. Wong, A. M. H. & Eleftheriades, G. V. An optical super-microscope for far-field, real-time imaging beyond the diffraction limit. *Sci. Rep.* **3**, 1715 (2013).

12. Baumgartl, J., Kosmeier, S., Mazilu, M., Rogers, E. T. F., Zheludev, N. I. & Dholakia, K. Far field subwavelength focusing using optical eigenmodes. *Appl. Phys. Lett.* **98**, 181109 (2011).

13. Piché, K., Leach, J., Johnson, A. S., Salvail, J. Z., Kobobov, M. I. & Boyd, R. W. Experimental realization of optical eigenmode super-resolution. *Opt. Express* **20**, 26424 (2012).

14. Lindberg, J. Mathematical concepts of optical superresolution. *J. Opt* **14**, 083001 (2012).

15. Amineh, R. K. & Eleftheriades, G. V. 2D and 3D sub-diffraction source imaging with a superoscillatory filter. *Opt. Express* **21**, 8142–8156 (2013).

16. Roy, T., Rogers, E. T. F. & Zheludev, N. I. Sub-wavelength focusing meta-lens. *Opt. Express* **21**, 7577 (2013).

17. Huang, F. M., Chen, Y. F., de Abajo, F. J. G. & Zheludev, N. I. Optical super-resolution through super-oscillations. *J. Opt. A: Pure Appl. Opt.* **9**, S285–S288 (2007).

18. Huang, F. M., Zheludev, N. I., Chen, Y. & de Abajo, F. Focusing of light by a nanohole array. *Appl. Phys. Lett.* **90**, 091119 (2007).

19. Huang, F. M., Kao, T. S., Fedotov, V. A., Chen, Y. & Zheludev, N. I. Nanohole array as a lens. *Nano. Lett.* **8**, 2469–2472 (2008).

20. Rogers, E. T. F., Lindberg, J., Roy, T., Savo, S., Chad, J. E., Dennis, M. R. & Zheludev, N. I. A super-oscillatory lens optical microscope for subwavelength imaging. *Nat. Mater.* **11**, 432–435 (2013).

21. Rogers, E. T. F., Savo, S., Lindberg, J., Roy, T., Dennis, M. R. & Zheludev, N. I. Super-oscillatory optical needle. *Appl. Phys. Lett.* **102**, 031108 (2013).

22. Roy, T., Rogers, E. T. F., Yuan, G. H. & Zheludev, N. I. Point spread function of the optical needle super-oscillatory lens. *Appl. Phys. Lett.,* **104**, 231109 (2014).

23. Rogers, E. T. F. & Zheludev, N. I. Optical super-oscillations: sub-wavelength light focusing and super-resolution imaging. *J. Opt.* **15**, 094008 (2013).

24. Ye, H. P., Qiu, C. W., Huang, K., Teng, J. H., Luk'yanchuk, B. & Yeo, S. P. Creation of a longitudinally polarized subwavelength hotspot with an ultra-thin planar lens: vectorial Rayleigh-Sommerfeld method. *Laser Phys. Lett.* **10**, 065004 (2013).

25. Liu, T., Tan, J. B., Liu, J. & Wang, H. T. "Vectorial design of super-oscillartory lens. *Opt. Express* **21**, 15090–15101 (2013).

26. Zhao, Y. Q., Edgar, J. S., Jeffries, G. D. M., McGloin, D. & Chiu, D. T. Spin-to-orbital angular momentum conversion in a strongly focused optical beam. *Phys. Rev. Lett.* **99**, 073901 (2007).

27. Zhan, Q. W. Properties of circularly polarized vortex beams. *Opt. Lett.* **31**, 867–869 (2006).

28. Wei, J. S., Zha, Y. K. & Gan, F. X. Creation of super-resolution non-diffraction beam by modulating circularly polarized light with ternary optical element. *Prog. Electromagn. Res.* **140**, 589–598 (2013).

29. Wang, H. F., Shi, L. P., Luk'yanchuk, B., Sheppard, C. & Chong, C. T. Creation of a needle of longitudinally polarized light in vacuum using binary optics. *Nat. Photon.* **2**, 501–505 (2008).

30. Yuan, G. H., Wei, S. B. & Yuan, X. C. Nondiffracting transversally polarized beam. *Opt. Lett.* **36**, 3479–3481 (2011).

31. Huang, K., Shi, P., Kang, X. L., Zhang, X. B. & Li, Y. P. Design of DOE for generating a needle of a strong longitudinally polarized field. *Opt. Lett.* **35**, 965–967 (2010).

32. Wang, H. F. & Gan, F. X. High focal depth with a pure-phase apodizer. *Appl. Opt.* **40**, 5658–5662 (2001).

33. Aieta, F., Genevet, P., Kats, M. A., Yu, N. F., Blanchard, R., Gaburro, Z. & Capasso, F. Aberration-free ultrathin flat lenses and axicons at telecom wavelengths based on plasmonic metasurfaces. *Nano Lett.* **12**, 4932–4936 (2012).

34. Ni, X. J., Ishii, S., Kildishev, A. V. & Shalaev, V. M. Ultra-thin, planar, Babinet-inverted plasmonic metalenses. *Light: Sci. Appl.* **2**, e72 (2013).

35. Chen, X. Z., Huang, L. L., Mühlenbernd, H., Li, G. X., Bai, B. F., Tan, Q. F., Jin, G. F., Qiu, C. W., Zhang, S. & Zentgraf, T. Dual-polarity plasmonic metalens for visible light. *Nat. Commun.* **3**, 1198 (2012).

36. Hecht, E. Optics. 3rd ed., Addison Wesley Publishing Company: Reading, MA, (1997).

37. Kotlyar, V. V., Stafeev, S. S., O'Faolain, L. & Soifer, V. A. Tight focusing with a binary microaxicon. *Opt. Lett.* **36**, 3100–3102 (2011).

38. Ishii, S., Shalaev, V. M. & Kildishev, A. V. Holey-metal lenses: sieving single modes with proper phases. *Nano Lett.* **13**, 159–163 (2013).

39. Gao, H. W., Hyun, J. K., Lee, M. H., Yang, J. C., Lauhon, L. J. & Odom, T. W. Broadband plasmonic microlenses based on patches of nanoholes. *Nano Lett.* **10**, 4111–4116 (2010).

40. Lezec, H. J., Degiron, A., Devaux, E., Linke, R. A., Martin-Moreno, L., Garcia-Vidal, F. J. & Ebbesen, T. W. Beaming light from a subwavelength aperture. *Science* **297**, 820–822 (2002).

41. Yuan, G. H., Rogers, E. T. R., Roy, T., Shen, Z. X. & Zheludev, N. I. Flat super-oscillatory lens for heat-assisted magnetic recording with sub-50 nm resolution. *Opt. Express* **22**, 6428–6437 (2014).

42. Tang, Y. Q. & Cohen, A. E. Enhanced enantioselectivity in excitation of chiral molecules by superchiral light. *Science* **332**, 333–336 (2011).

43. Jin, N. & Rahmat-Samii, Y. Advances in particle swarm optimization for antenna designs: Real-number, binary, single-objective and multiobjective implementations. *IEEE Trans. Antenn. Propag.* **55**, 556–567 (2007).

44. Kotlyar, V. V. & Kovalev, A. A. Nonparaxial propagation of a Gaussian optical vortex with initial radial polarization. *J. Opt. Soc. Am. A* **27**, 372–380 (2010).

45. Grosjean, T. & Courjon, D. Polarization filtering induced by imaging system: effect on image structure. *Phy. Rev. E* **67**, 046611 (2003).

Acknowledgments

Author contributions

G.H.Y. carried out the optimization, conducted the fabrication and experiment, and prepared the manuscript. E.T.F.R. and T.R. assisted in the optimization and experiment. G.A. helped in fabricating the sample. N.I.Z. and Z.X.S. supervised and coordinated all of the work. All of the authors discussed the results and revised the manuscript extensively.

Additional information

Supplementary information accompanies this paper at http://www.nature.com/scientificreports

Competing financial interests: The authors declare no competing financial interests.

How to cite this article: Yuan, G. *et al.* Planar super-oscillatory lens for sub-diffraction optical needles at violet wavelengths. *Sci. Rep.* **4**, 6333; DOI:10.1038/srep06333 (2014).